Layer and Stacking Effects on Transport Properties in Steep-Slope Cold-Metal-Source FETs

Chiao-Yu Chang[1,2], Bart Sorée [1,2,3], and Aryan Afzalian[1]
[1] *Imec, Kapeldreef 75, 3001 Leuven, Belgium*
[2] *KU Leuven, Department of Electrical Engineering, Kasteelpark Arenberg 10, 3001 Leuven, Belgium*
[3] *University of Antwerp, Department of Physics, Antwerpen B-2020, Belgium*
chiao-yu.chang@imec.be

***Abstract*—We investigate the impacts of layer number and heterostructure stacking on the transport of 2D cold-metal-source FETs within the DFT-NEGF framework using our NEGF solver, ATOMOS, which enables electron-phonon coupling analysis. Our simulations demonstrate that optimized NbS_2/WS_2 stacking reduces the van der Waals gap, enhancing on-current, while additional cold-metal layers introduce density of states near the Fermi level, further improving the on-current. This study presents an effective design strategy for cold-source materials and contacts to achieve steep-slope transport.**

***Index Terms*—cold metal, DFT NEGF, metal-semiconductor interface, 2D material, device modeling**

I. Introduction

Low-power transistors have long been a key focus of semiconductor development. The efficiency of conventional FETs is limited by the subthreshold swing (SS) $\geq$ 60 mV/decade. A primary mechanism is that the thermal tail, originating from high-energy carrier states at the source, facilitates hot carriers to cross the channel barrier. To overcome the challenge, several steep-slope field-effect transistor (FET) designs were proposed, such as tunnel FET, negative capacitance FETs, Dirac-source FETs (DSFET), and cold-source FETs (CSFETs) [1]. Dirac-source FET utilizes the unique density of states (DOS) feature of Dirac materials, such as graphene, which serves as a source contact material to reduce the hot carriers across the channel barrier in the subthreshold region and exhibits subthermionic SS and high I_{ON} with negligible hysteresis [1]–[4]. Similarly, CSFET takes advantage of the energy gap(s) around the Fermi level (E_F) to filter hot carriers [4]. Since the fabrication of the first DSFET in 2018, extensive theoretical research has explored DSFETs and CSFETs, such as 2D-DSFETs using graphene/MoS_2 [1] and CSFETs based on two-dimensional transition-metal dichalcogenides (TMDs) [5]–[8], MXenes [7], 1D carbon nanotubes [9], or silicon [10]. However, few studies have taken electron-phonon coupling (e-ph) into consideration. Here, we employed TMDs as our material combination, which are intrinsically 2D in nature and are reported to have dangling-bond-free surfaces and a wide variety of physical properties. The former quality helps avoid Fermi-level pinning [7], while the latter broadens material selection flexibility. The cold metal, 2H-NbS_2, is one of the TMDs possessing a fascinating band structure with an isolated Nb-4d band sandwiched by two energy gaps, which can efficiently cut off the thermal tail. The E_F is located in this band, rendering 2H-NbS_2 metallic [5], [8]. We choose 2H-NbS_2 as the source material and WS_2 as the channel material, employing the DFT-NEGF method to investigate the effects of stacking configurations and layer numbers on transport properties and evaluate the impact of e-ph.

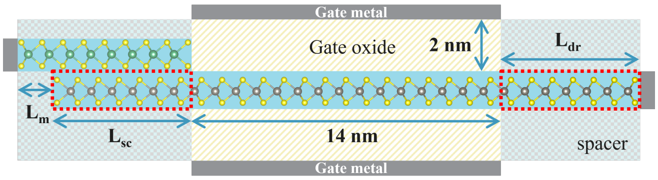

Fig. 1. The schematic of the double-gate cold-source FET structure.

II. Methods

We performed ab initio simulations within density functional theory (DFT) and the non-equilibrium Green's function (NEGF) formalism. Firstly, we carried out DFT calculations on the TMD monolayers and heterojunctions using QUANTUM ESPRESSO [11] with ultrasoft pseudopotentials, and the optB86b-vdW exchange correlation functional was applied in which the nonlocal effects of van der Waals (vdW) interactions were described [12], enabling a more accurate modeling of interlayer distance (d_{inter}, also referred to as the vdW gap here). A well-converged kinetic energy cut-off of the plane-wave basis of 70 Ry was selected. The K space was sampled using a $10 \times 10 \times 1$ Monkhorst-Pack (MP) grid for relaxation and self-consistent calculations and a denser $30 \times 30 \times 1$ MP grid for electronic structure calculations. The primitive cells were fully relaxed with a convergence threshold of 10^{-5} Ry on the total energy for each ionic minimization and a threshold of 10^{-4} Ry/Bohr on forces. Then, we combined two unit cells to form supercells (SCs) and fully relaxed the SCs to obtain the most stable structures.

Secondly, Wannier90 was employed to convert the plane-wave basis to maximally-localized Wannier functions [13] and to construct the device Hamiltonian for NEGF simulations. The d orbitals of the transition metals and the p orbitals of

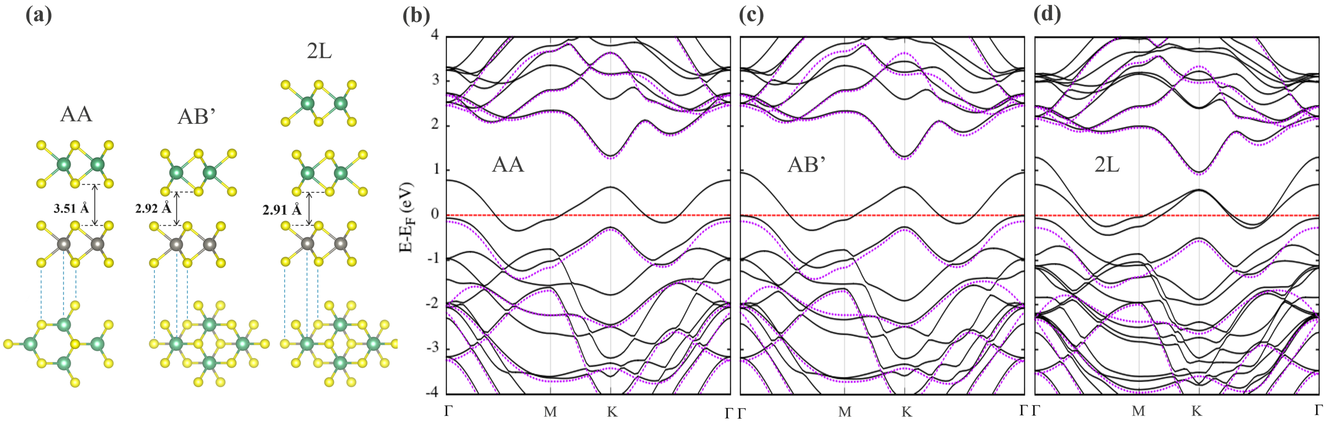

Fig. 2. (a) Atomic structures of relaxed AA-stacked (left), AB'-stacked (middle), and bilayer (2L) NbS_2/WS_2 (right) heterostructures, with NbS_2 as the top layer and WS_2 as the bottom layer. Corresponding top-view schematics are shown below each structure. (b–d) Electronic band structures of the (b) AA-stacked, (c) AB'-stacked, and (d) 2L NbS_2/WS_2 heterostructures. The red dashed lines denote the E_F of heterostructures, and the purple dashed curves represent the band structures of freestanding WS_2 with the same lattice constants as the corresponding heterostructures.

sulfurs were chosen as initial projections during the wannierization since these orbitals dominate the transport properties.

Finally, we conducted NEGF simulations using our advanced ATOmistic Modeling Solver (ATOMOS) [14]. ATOMOS allows us to perform dissipative simulations with e-ph analyses, combined with the Message Passing Interface (MPI) standard, to achieve parallel computing on a high-performance computing system for heavy Hamiltonian matrix calculations. We constructed the 2D double-gate CSFET, as shown in Fig. 1, with different metal-semiconductor stackings and cold-source layer numbers. The optimized source contact length (L_{sc}) and drain extension length (L_{dr}) of about 4.90 nm and the source metal extension length (L_m) of about 1.95 nm were used. The p-doping concentration was $1.86 \times 10^{13} cm^{-2}$ in the source contact and drain extension, as marked regions inside the red dashed lines in Fig. 1.

III. RESULTS

In this work, we investigated the energies, relaxed atomic structures, and electronic structures of five different NbS_2/WS_2 stackings: AA, AB, AA', AB', and A'B. Then, we selected the case with the smallest vdW gap for more in-depth DFT and quantum transport analyses and compared it with the case having the largest d_{inter} to demonstrate the d_{inter}'s effect, and examine the electron-phonon coupling effects in both configurations. Finally, we studied the influences of the additional NbS_2 layer on transport.

We initially compared the energies and relaxed atomic structures of five stackings. The results show negligible energy differences (about 11.34 meV/atom) among the five stacking configurations, suggesting that no single stacking is clearly more energetically stable than the others. As for relaxed heterostructures, the smallest d_{inter} of 2.92 Å was found in the AB' case. This is pronouncedly shorter than 3.51 Å, the d_{inter} of AA stacking (by 0.59 Å), as illustrated in Fig. 2 (a). A shorter vdW interlayer distance leads to enhanced wavefunction overlap between adjacent layers, increased interlayer hopping probability of electrons or holes, and reduced interlayer tunneling barrier. Therefore, we selected the AA- and AB'-stacked configurations for subsequent investigations with the aim of elucidating the effects induced by the significantly reduced interlayer distance. Table I summarizes the remaining biaxial strains ($\varepsilon_{\parallel}$) in each layer (resulting from the initial commensuration of the cells and their subsequent relaxation), WS_2 band gaps (E_g), and contact type (or Schottky barriers, Φ_{sh}) in both cases.

TABLE I
SUMMARY OF STRAIN, INTERLAYER DISTANCE, BAND GAP, AND CONTACT TYPE

Stacking	d_{inter}	$\varepsilon_{\parallel}^{NbS_2}$	$\varepsilon_{\parallel}^{WS_2}$	E_g	Contact Type
AA	3.51 Å	-1.89%	2.93%	1.39 eV	$\Phi_{sh} = 64.8$ meV
AB'	2.92 Å	-1.84%	2.98%	1.32 eV	Ohmic
2L	2.91 Å	-1.68%	3.84%	1.03 eV	$\Phi_{sh} = 62.7$ meV

To further assess the interlayer coupling, the electronic band structures of AA- and AB'-stacked NbS_2/WS_2 were calculated and presented in Fig. 2 (b-c). After forming heterostructures, the E_g values of WS_2 in the heterostructures are reduced and become indirect due to the transition of the valence band maximum (VBM) from the K point to the Γ point, given that the unstrained monolayer WS_2 has a direct E_g of 1.94 eV, according to our DFT results. These effects are primarily caused by tensile strain in the WS_2 layer, as verified by the identical strain-induced band structure modifications observed in isolated WS_2 under equivalent strain conditions [see the purple dashed curves in Fig. 2 (b-c)]. Compared to the strained WS_2 band structures, the VBM energy shifts and band structure distortion indicate stronger interlayer coupling in the AB' configuration compared to AA.

The I_{DS}-V_G characteristics of AA- and AB'-stacked CS-

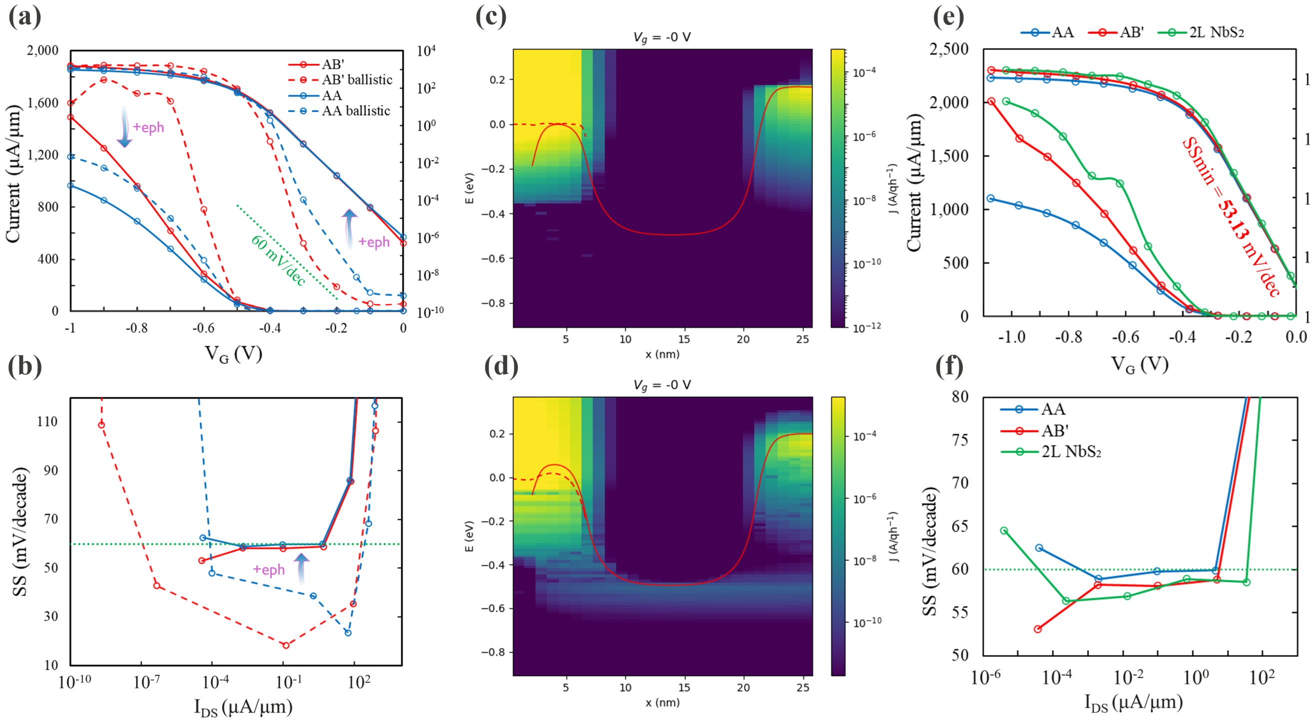

Fig. 3. NEGF simulation results of p-type CSFETs with a channel length of 14 nm and $V_D = -0.15V$. (a) I_{DS}-V_G curves and (b) Subthreshold swing versus I_{DS} relation of AA and AB' CSFETs with e-ph (solid lines) and without scattering (dashed lines). Current density spectra of AB'-stacked CSFET at V_G = 0V (c) without e-ph and (d) with e-ph. The red dashed curves in the current spectra represent the E_F of the cold source, and the solid curves represent the VBM of WS$_2$. (e) I_{DS}-V_G curves with I_{OFF} fixed at 100 pA/μm and (f) SS as a function of I_{DS} of AA, AB', and 2L configurations, including e-ph. The green dashed lines denote the thermionic limit of 60 mV/dec. The current is normalized per μm of device width.

FETs are presented in Fig. 3(a). Compared to AA stacking, AB' stacking enhances I_{ON}, whether the scattering is included or not. We attribute this improvement to the substantially reduced d_{inter}, as a shorter vdW gap and increased interlayer coupling increase the probability of carriers tunneling through the vdW barrier [15]. The impacts of e-ph in both cases are also shown in Fig. 3(a) and 3(b), where it is evident that scattering significantly degrades device performance. The I_{ON} is reduced, while the off-state leakage current increases as a result of scattering. The reason is that when low-energy carriers enter WS$_2$, where high-energy carrier states are available, these cold carriers can regain the energy from the phonon to overcome the channel barrier in the subthreshold region. This phenomenon can be verified by the current density spectrum [Fig. 3 (d)], where the cold holes are rethermalized by e-ph, resulting in the leakage current in the off state. Consequently, the SS increases considerably in both cases. Nevertheless, the AB'-stacked device exhibits a lower SS$_{min}$ of 53.13 mV/dec and a broader sub-60 mV/dec current range than the AA-stacked counterpart.

Ballistically, in the off-state, these low-energy carriers would remain in their initial energies, preventing carrier injection over the barrier, as demonstrated in Fig. 3 (c), leading to lower leakage current and lower SS. SS can also be improved by stacking in the ballistic limit, from 23.37 mV/dec in AA stacking to 18.31 mV/dec in AB' case, and the sub-60 mV/dec current range also expands from about seven current decades to about nine decades due to the different stacking.

Our electron-phonon coupling analysis further confirms that e-ph is the primary factor limiting the subthreshold swing in CSFETs. For future CSFET research, we propose focusing on mitigating phonon scattering effects to enhance device performance.

Finally, we further explore the effects of an additional NbS$_2$ layer on the transport of the CSFET. Figure 2 (a) shows the relaxed atomic heterostructure, and the results show the d_{inter} in the bilayer (2L) NbS$_2$/WS$_2$ structure is nearly identical to that of the monolayer case in AB' stacking. Regarding strain, from Table I, a greater portion is distributed to the WS$_2$ layer, resulting in a more pronounced strain-induced reduction in the band gap of WS$_2$. However, this does not affect the normal switching operation of the device. The electronic structure of the 2L arrangement was also calculated, as shown in Fig. 2 (d). A larger variation in VBM energy upon heterostructure formation, relative to the other cases, reflects stronger interlayer coupling between 2L-NbS$_2$ and WS$_2$.

Figure 3 (e) and 3 (f) show the NEGF simulation results after increasing the number of NbS$_2$ layers with I_{OFF} fixed at 100 pA/μm, compared with the AA and AB' stackings. The switching performance is improved. Especially for I_{ON}, the added NbS$_2$ layer provides a higher DOS near the E_F due to an extra d-band introduced by additional NbS_2 layer as shown in Fig. 2 (d), thus increasing the carrier concentration that can be injected in the on-state.

IV. CONCLUSIONS

This study investigates the influence of layer number and heterostructure stacking on the transport properties of steep-slope CSFETs using a DFT-NEGF approach. The results reveal that AB' stacking noticeably enhances I_{ON} due to a reduced vdW gap, facilitating carrier injection. Furthermore, increasing the number of NbS_2 layers further optimizes the device performance by increasing the density of states near the E_F, providing more carriers injected into the source, thus improving I_{ON}. However, electron-phonon interactions introduce performance degradation, increasing the SS and leakage current, and are further identified as the dominant factor hindering the realization of sub-60 mV/dec SS in CSFETs. These findings provide insights into material selection and device engineering strategies for achieving sub-60 mV/dec transistors.

V. ACKNOWLEDGMENT

This work has received funding from the European Commission-EU Attoswitch project under grant agreement n. 101135571.

REFERENCES

[1] F. Liu, C. Qiu, Z. Zhang, L.-M. Peng, J. Wang, and H. Guo, "Dirac electrons at the source: Breaking the 60-mv/decade switching limit," *IEEE Transactions on Electron Devices*, vol. 65, no. 7, pp. 2736–2743, 2018.

[2] C. Qiu, F. Liu, L. Xu, B. Deng, M. Xiao, J. Si, L. Lin, Z. Zhang, J. Wang, H. Guo *et al.*, "Dirac-source field-effect transistors as energy-efficient, high-performance electronic switches," *Science*, vol. 361, no. 6400, pp. 387–392, 2018.

[3] S. Wang, J. Wang, T. Zhi, J. Xue, D. Chen, L. Wang, and R. Zhang, "Cold source field-effect transistors: Breaking the 60-mv/decade switching limit at room temperature," *Physics Reports*, vol. 1013, pp. 1–33, 2023.

[4] F. Liu, C. Qiu, Z. Zhang, L.-M. Peng, J. Wang, Z. Wu, and H. Guo, "First principles simulation of energy efficient switching by source density of states engineering," in *2018 IEEE International Electron Devices Meeting (IEDM)*. IEEE, 2018, pp. 33–2.

[5] F. Liu, "Switching at less than 60 mv/decade with a "cold" metal as the injection source," *Physical review applied*, vol. 13, no. 6, p. 064037, 2020.

[6] Q. Wang, P. Sang, X. Ma, F. Wang, W. Wei, W. Zhang, Y. Li, and J. Chen, "Cold source engineering towards sub-60mv/dec p-type field-effect-transistors (pfets): Materials, structures, and doping optimizations," in *2020 IEEE International Electron Devices Meeting (IEDM)*. IEEE, 2020, pp. 22–4.

[7] J. Lyu, J. Pei, Y. Guo, J. Gong, and H. Li, "A new opportunity for 2d van der waals heterostructures: making steep-slope transistors," *Advanced Materials*, vol. 32, no. 2, p. 1906000, 2020.

[8] Y. Yin, Z. Zhang, C. Shao, J. Robertson, and Y. Guo, "Computational study of transition metal dichalcogenide cold source mosfets with sub-60 mv per decade and negative differential resistance effect," *npj 2D Materials and Applications*, vol. 6, no. 1, p. 55, 2022.

[9] L. Xu, K. Luo, G. Zhan, X. Feng, H. Yang, Y. Liu, J. Liu, Q. Xu, H. Yin, and Z. Wu, "Realization of steep-slope transistor using 1-d gate-all-around carbon nanotubes with broken-gap source structure," *IEEE Transactions on Electron Devices*, 2024.

[10] H. Zhou, X. Dong, R. J. Prentki, R. Cao, J. Wang, H. Guo, and F. Liu, "Quantum transport simulations of sub-60-mv/decade switching of silicon cold source transistors," *IEEE Transactions on Electron Devices*, 2024.

[11] P. Giannozzi, S. Baroni, N. Bonini, M. Calandra, R. Car, C. Cavazzoni, D. Ceresoli, G. L. Chiarotti, M. Cococcioni, I. Dabo *et al.*, "Quantum espresso: a modular and open-source software project for quantumsimulations of materials," *Journal of physics: Condensed matter*, vol. 21, no. 39, p. 395502, 2009.

[12] J. Klimeš, D. R. Bowler, and A. Michaelides, "Van der waals density functionals applied to solids," *Physical Review B—Condensed Matter and Materials Physics*, vol. 83, no. 19, p. 195131, 2011.

[13] A. A. Mostofi, J. R. Yates, G. Pizzi, Y.-S. Lee, I. Souza, D. Vanderbilt, and N. Marzari, "An updated version of wannier90: A tool for obtaining maximally-localised wannier functions," *Computer Physics Communications*, vol. 185, no. 8, pp. 2309–2310, 2014.

[14] A. Afzalian, "Ab initio perspective of ultra-scaled cmos from 2d-material fundamentals to dynamically doped transistors," *npj 2D Materials and Applications*, vol. 5, no. 1, p. 5, 2021.

[15] A. Afzalian, E. Akhoundi, G. Gaddemane, R. Duflou, and M. Houssa, "Advanced dft–negf transport techniques for novel 2-d material and device exploration including hfs 2/wse 2 van der waals heterojunction tfet and wte 2/ws 2 metal/semiconductor contact," *IEEE Transactions on Electron Devices*, vol. 68, no. 11, pp. 5372–5379, 2021.